The Time Scales of Variability of Marine Low Clouds

Simon P. de Szoeke and Kathryn L. Verlinden

Oregon State University, Corvallis, Oregon

Sandra E. Yuter

North Carolina State University, Raleigh, North Carolina

David B. Mechem

University of Kansas, Lawrence, Kansas

ABSTRACT

Multidecade global regressions of inversion strength, vertical velocity, and sea surface temperature (SST) on low cloud amount, from subdaily to multiyear time scales, refute the dominance of seasonal inversion strength on marine low cloud variability. Multiday low cloud variance averaged over the eastern Pacific and Atlantic stratocumulus regions [5×10^{-2} (cloud amount)^2] is twice the subdaily variance and 5 times larger than the multimonth variance. The broad multiday band contains most (60%) of the variance, despite strong seasonal (annual) and diurnal spectral peaks. Multiday low cloud amount over the eastern tropical and midlatitude oceans is positively correlated to inversion strength, with a slope of 2%–5% K^{-1}. Anecdotes show multiday low cloud and inversion strength anomalies propagate equatorward from midlatitudes. Previously shown correlations of low clouds to strong inversions and cool SST on monthly and longer time scales in the stratocumulus regions imply positive cloud-radiative feedbacks, with e-folding time scales of 300 days for SST and 14 days for atmospheric boundary layer temperature. On multimonth time scales, removing the effect of SST on low clouds reduces the low cloud amount explained by inversion strength by a factor of 3, but SST has a small effect at other time scales. Contrary to their positive correlation in the stratocumulus cloud decks, low clouds are anticorrelated to inversion strength over most of the tropics on daily and subdaily time scales.

1. Introduction

By reflecting solar radiation and emitting thermal radiation at a temperature close to that of the surface, marine low clouds have a net cooling effect on the climate. The response of low clouds and their associated radiative effect in a changed climate is the leading source of uncertainty for future climate projection (Bony and Dufresne 2005). The climate sensitivities projected by climate models differ considerably and depend on the response of low cloud amount to SST (Lauer et al. 2010). Understanding how low cloud amount depends on predictable aspects of the atmospheric circulation is essential to quantifying the surface temperature response to climate change forced by long-lived greenhouse gas emissions.

Marine low clouds are prevalent (low cloud amount >0.6) over relatively cool sea surfaces poleward of 40° latitude and across the subtropical and tropical eastern oceans. The southeastern subtropical Indian Ocean, northeastern subtropical Pacific Ocean, and the southeastern tropical Pacific and Atlantic Oceans have persistent marine low cloud decks (Fig. 1b). Greater stratocumulus cloud amount is found in these decks for cooler sea surface temperature (SST; e.g., Tselioudis et al. 1992;

Corresponding author address: Simon P. de Szoeke, College of Earth, Ocean, and Atmospheric Sciences, Oregon State University, 104 CEOAS Admin. Building, Corvallis, OR 97331.
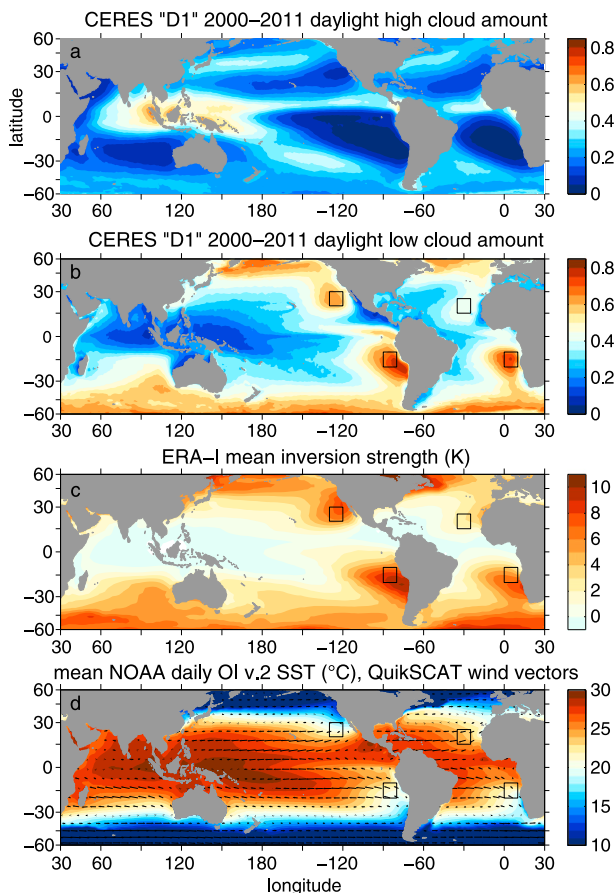E-mail: sdeszoek@coas.oregonstate.edu

FIG. 1. Mean (a) high cloud amount ($p_{top} < 560$ hPa) from the CERES daylight ISCCP D1-like cloud mask, (b) low cloud amount ($p_{top} > 560$ hPa), (c) inversion strength from ERA-I, and (d) NOAA daily OISSTv2 (Reynolds et al. 2007), and year-round climatological wind vectors from the QuikSCAT Scatterometer Climatology of Ocean Winds (SCOW; Risien and Chelton 2008). A $1 \, m \, s^{-1}$ wind vector is scaled to a length of 1° of longitude. Squares show the locations of tropical and subtropical marine low cloud averaging regions identified by KH93. The latitude axis is proportional to the sine of latitude, so area is preserved.

Clement et al. 2009; Lauer et al. 2010) and for more stable lower troposphere (Klein and Hartmann 1993, hereafter KH93) and atmospheric boundary layer (ABL) inversions (Wood and Bretherton 2006). Increased subsidence leads to greater low cloud amount if it sufficiently increases the inversion strength. However, for a given inversion strength, stronger subsidence over the stratus deck reduces the low cloud amount in monthly average data (Myers and Norris 2013).

Low stratiform clouds depend on whether the water vapor is saturated at the top of the boundary layer, which in turn is a delicate balance of moisture flux from the sea surface and entrainment of dry, free-tropospheric air. Greater inversion stability increases the energetic cost for turbulence to entrain dry air. A smaller entrainment rate

reduces drying of the ABL and maintains the cloud near saturation. In the semipermanent stratocumulus cloud deck over the southeastern Pacific, synoptic variations of the lower free-tropospheric temperature affect the inversion strength and the propensity for the boundary layer to entrain dry air and reduce its cloud cover (Toniazzo et al. 2011; Rozendaal and Rossow 2003).

To ameliorate climate model bias in mean low cloud amount, some low cloud parameterizations have used the well-known relationship between seasonal mean cloud amount and stability [specifically, the increase of 0.06 low cloud amount per kelvin of lower-tropospheric stability, measured by the difference in potential temperature between 700 and 1000 hPa (KH93)]. For example, one parameterization directly prescribes low cloud amount according to this seasonal relationship (Rasch and Kristjánsson 1998), and another uses a stability threshold to determine whether to activate a shallow cumulus parameterization (Dee et al. 2011). The seasonal relationship between low cloud amount and stability is unlikely to be physically appropriate at the typical general circulation model grid scale and time step. Even using the relationship for the straightforward purpose of correcting mean daily solar radiation incident on the ocean surface may disrupt important cloud–SST interactions, since cloud properties may take several days to respond to SST anomalies (Klein et al. 1995; Xu et al. 2005).

An analogous relationship to the seasonal correlation of low clouds to lower-tropospheric stability on time scales other than seasonal is not well understood. Klein (1997) studied synoptic variability of cloud and meteorology observations at Ocean Weather Station November in the Pacific Ocean (30°N, 140°W), finding that boundary layer clouds are associated with cold advection, lower-tropospheric stability, humidity, strong wind speed and stress, strong sensible and latent heat fluxes, well-coupled boundary layers, sea level pressure (SLP) ridges, subsidence, and deeper atmospheric boundary layers; but none of these explains more than 13% of low cloud variance on daily time scales. Lower-tropospheric stability and cold advection explain more variance than most variables, and the variance explained increases when the daily data are averaged over tens of days (Klein 1997; Kubar et al. 2012, hereafter KWLJ12). Low cloud amount increases when SLP ridges align poleward of the cloud region (Klein 1997; Rozendaal and Rossow 2003; George and Wood 2010). Low-frequency variability, such as El Niño–Southern Oscillation (ENSO), modulates the relationship on daily time scales between low cloud amount and lower-tropospheric stability (Sun et al. 2011).

This work examines the subdaily to multiyear time scales of low cloud variability over all of Earth's ice-free

oceans. From a global perspective, we compare the influence of inversion strength, SST, and vertical velocity on low clouds among regions and time scales. We examine the variability of low clouds from 26.5 years of 3-hourly infrared satellite cloud observations from the International Satellite Cloud Climatology Project (ISCCP; Rossow and Schiffer 1999; ISCCP Science Team 1999). In section 2, we describe the ISCCP dataset, the European Centre for Medium-Range Forecasts interim reanalysis (ERA-Interim; Dee et al. 2011), and the National Oceanic and Atmospheric Administration (NOAA) Optimum Interpolation SST version 2 product (OISSTv2; Reynolds et al. 2007). The dataset descriptions include details about the methods used to estimate low cloud variability and address ISCCP calibration drifts and biases among satellites. Methods for analyzing the cloud variability at different time scales and its slope with respect to inversion strength, vertical velocity, and SST are described in section 3. We compare variability of the low clouds, SST, and inversion strength on subdaily, multiday, multimonth, and multiyear time scales in section 4. In section 5, we discuss the response of clouds to inversion strength, SST, and vertical velocity. In section 6, we describe multiday equatorward-propagating anomalies of inversion strength and low clouds. In section 7, we estimate radiative feedbacks to the atmospheric boundary layer temperature and SST from the observed response of low clouds to inversion strength and SST on different time scales. Section 8 concludes the paper with a summary.

2. Data

a. Low cloud amount

Low cloud amount is calculated from the 26.5-yr record of the 3-hourly, equal-area ($280 \times 280\,\mathrm{km}^2$) ISCCP D1 gridded product (Rossow and Schiffer 1999). We use the ISCCP data at times that correspond to the 6-hourly reanalysis data. The D1 gridded data count the number of satellite fields of view (4–7-km radius pixels) whose radiances correspond to given cloud properties within the $280 \times 280\,\mathrm{km}^2$ spatial grid and time interval. Cloud amount (fraction) is defined as the number of cloud pixels divided by the total number of pixels observed. To ensure consistent sampling over the diurnal cycle, we use only infrared cloud retrievals. Instead of the standard ISCCP low cloud boundary of 680 hPa, we define low clouds as having cloud-top pressure greater than (altitude below) 560 hPa in order to include boundary layer clouds that may have tops that extend to higher altitude. Clouds defined by this cloud-top pressure include shallow cumulus in the tropics and clouds above the ABL in midlatitudes.

Results are relatively insensitive to using the low cloud amount for each ISCCP scene assuming a random-overlap distribution of clouds with height. The random-overlap adjusted low cloud amount represents the fraction of low clouds observed when high clouds do not obscure the satellite view of the low clouds (Rozendaal et al. 1995).

The ISCCP cloud anomalies and their long-term means are affected by changes in viewing angle and satellite calibration. To correct for viewing angle artifacts, for each satellite we subtract cloud amount anomalies correlated to satellite view angle. To address satellite calibration drift, for each location and time we remove the regression of the low cloud amount with the low cloud amount mean over the entire view of the satellite (Norris 2000, 2005; Norris and Evan 2015). The long-term mean is not preserved by subtracting the regressions on viewing angle and mean satellite view, so the analysis is carried out only on anomalies. Mean daylight high and low cloud amount (Figs. 1a and 1b, respectively; separated by cloud-top pressure $p_{\mathrm{top}} = 560\,\mathrm{hPa}$) are from 2000–11 infrared and visible radiances from the Clouds and the Earth's Radiant Energy System (CERES) ISCCP D1-like satellite cloud amount product (Wielicki et al. 1996; Loeb et al. 2009).

b. Inversion strength and vertical velocity

Inversion strength [estimated inversion strength (EIS; Wood and Bretherton 2006)] is computed from 6-hourly ERA-Interim (hereafter ERA-I; Dee et al. 2011) fields. EIS estimates cloud base from the 1000-hPa potential temperature and humidity. Potential temperature is assumed constant (adiabatic) below cloud base and is assumed to follow the moist adiabatic lapse rate both in the ABL cloud and in the free troposphere. The moist adiabatic lapse rate is computed from the 850-hPa air temperature.

The EIS calculation (Wood and Bretherton 2006) is not intended for regions dominated by deep convection. Nevertheless, EIS indicates the lower-tropospheric stability, independent of changes in the moist adiabatic lapse rate.

We use vertical pressure velocity at 700 hPa ω_{700} from the 6-hourly ERA-I. Vertical velocity has a semidiurnal zonally propagating atmospheric tide at the Nyquist frequency of the 6-hourly reanalysis sampling. It is resolved strongly at some longitudes and weakly at others. To avoid aliasing the semidiurnal tide on subdaily time scales, we diagnose its average phase and latitude-dependent amplitude and remove it from the ω_{700} time series.

c. Sea surface temperature

We use the ¼° daily NOAA OISSTv2 (Reynolds et al. 2007). The optimal interpolation procedure merges the Advanced Very High Resolution Radiometer infrared retrieval in clear air with microwave SST retrievals

beneath clouds. NOAA OISSTv2 is not biased by clouds because the SST is retrieved from the microwave regardless of clouds.

3. Methods

We examine the magnitude of low cloud variability at multiyear, multimonth, multiday, and subdaily time scales; and the regression of low cloud amount with inversion strength, SST, and vertical velocity for anomalies averaged over these same time scales. The input data are 6-hourly time series of ISCCP low cloud amount c, ERA-I inversion strength s and 700-hPa vertical pressure velocity ω_{700}, and daily SST T, each averaged to the equal-area ($280 \times 280\,\mathrm{km}^2$) ISCCP grid points.

Data used in covariances are quality controlled according to two criteria: inversion strength must be positive, and high cloud amount (with $p_{\mathrm{top}} < 560\,\mathrm{hPa}$) must be less than 0.5. This focuses the analysis on ABL clouds observed below stable inversions. Excluding scenes with large high cloud amount from the covariances minimizes the influence of spurious correlations because of changes in high clouds. Regressions are not sensitive to the exact choice of the high cloud amount threshold. Random-overlap-adjusted low cloud covariances give similar results to low cloud amount covariances quality controlled by this procedure.

We define anomalies of c, s, T, and ω_{700} using four averaging windows to resolve 1) subdaily, 2) multiday, 3) multimonth, and 4) multiyear variability. The start and end of each averaging window is defined in UTC by the hour, day, month, or year of the civil calendar. These window-averaged anomalies are denoted $c^{6\mathrm{h}}$, c^{day}, c^{month}, and c^{year}, with the superscript denoting the time scale over which they are averaged. Appendix A formally defines the calendar window averages and shows that the window-average anomalies are mutually orthogonal. SST data are daily, so subdaily SST variability is not resolved. The periodic seasonal (annual) and diurnal cycles are diagnosed by compositing monthly averages by calendar month and 6-h averages by time of day, respectively.

Variances (σ^2) are computed for the anomalies of the full time series and each of the calendar window-average anomalies. We show the slopes m_{cs} of the regression of low cloud c on inversion strength s and m_{cT} of low cloud on SST (appendix B). For each time scale, we compute the low cloud amount anomalies predicted by their regression on inversion strength, SST, and vertical velocity.

4. Time scales of low cloud variability

Figure 2 shows the regional pattern of the standard deviation $\sigma(c)$ of ISCCP low cloud amount for the full
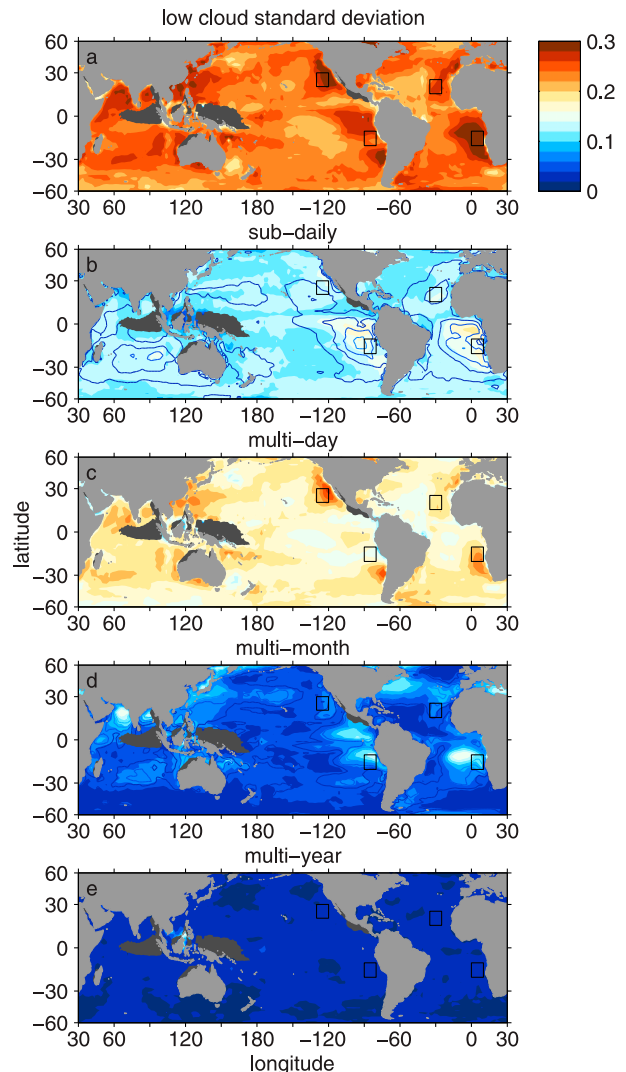

FIG. 2. (a) Standard deviation of low cloud amount ($p_{\mathrm{top}} > 560\,\mathrm{hPa}$) and standard deviation for the time series separated into (b) 6-hourly averages, (c) daily averages, (d) monthly averages, and (e) yearly averages. Unfilled contours in (b) and (d) represent the standard deviation of the periodic diurnal (day^{-1}) and seasonal (yr^{-1}) cycles, respectively. Unfilled contours in (d) differ from the multimonth standard deviation by less than one contour interval (0.02). Marine areas where the mean low cloud amount is less than 0.15 are masked with dark gray. Deep-convective clouds dominate these areas, and low cloud amount observed by satellite, and its variation, is affected by high clouds.

6-hourly time series and for the subday, multiday, multimonth, and multiyear window-averaged anomalies. The total standard deviation of low cloud amount is 0.2–0.3 over most of the oceans (Fig. 2a) and is highest over the eastern tropical and subtropical oceans, where low cloud amount is climatologically high (Fig. 1a). Low cloud amount has a "red" spectrum, with power weighted to low frequencies, but the higher-frequency
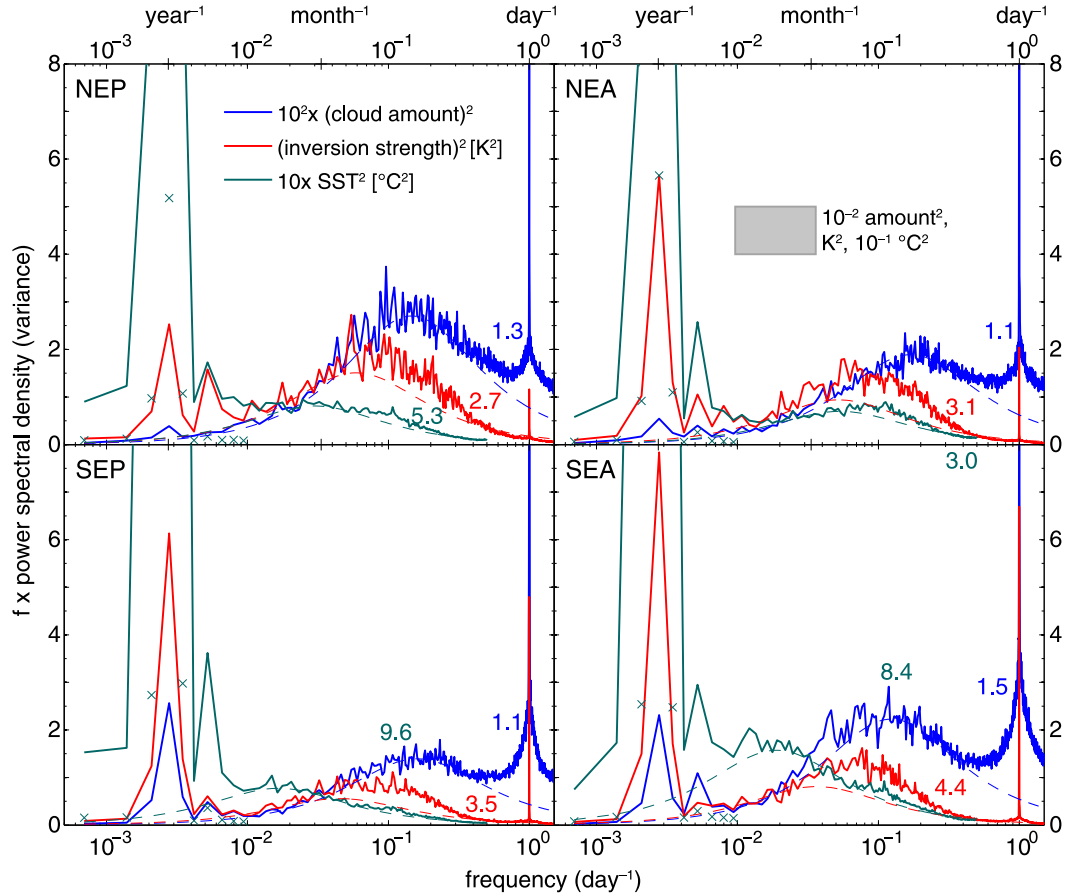
FIG. 3. Variance-preserving spectra of low cloud amount and inversion strength in the four eastern tropical or subtropical Pacific and Atlantic stratocumulus regions: NEP, NEA, SEP, and SEA. The gray-shaded rectangle in the panel labeled NEA illustrates the area that under the curve would represent variance of 10^{-2} (fractional amount)^2 low cloud, $1\,K^2$ inversion strength, and $10^{-1}°C^2$ SST. Crosses show the seasonal peak of SST variance on the same scale ($1\,K^2$) as inversion strength. Dashed lines are red noise fits to the portion of the respective spectra between the annual and daily peaks. The damping time scale τ (days) is printed beside the curves.

subdaily and multiday bands account for 87% of the total variance. The multiday standard deviation is $\sigma(c^{day}) = 0.2$ (Fig. 2c). Subdaily standard deviation $\sigma(c^{6h})$ ranges from 0.16 to 0.2 in the southeastern tropical Atlantic and Pacific Oceans. Multimonth standard deviation of low cloud amount $\sigma(c^{month})$ is about 0.1 over the eastern tropical and subtropical oceans and less elsewhere. Multiyear low cloud amount standard deviation $\sigma(c^{year})$ is very small (0.02–0.04) over most of the oceans. In the eastern Pacific and Atlantic stratocumulus regions, 57% of the variance is multiday, 30% is subdaily, 11% is multimonth, and <1% is multiyear.

The standard deviation of the climatological seasonal cycle $\sigma(c^{seasonal})$, shown as unfilled contours with the same color scale as the multimonth variability in Fig. 2d, constitutes about 90% of the total multimonth (periodic and aperiodic) standard deviation $\sigma(c^{month})$. The contours are difficult to see because they match the total

multimonth standard deviation $\sigma(c^{month})$. In contrast to the seasonal cycle, the periodic diurnal cycle explains a much smaller fraction (<10%) of the subdaily standard deviation (Fig. 2b).

We perform spectral analysis of low cloud amount c, inversion strength s, and SST T for the northeastern and southeastern Atlantic and Pacific stratocumulus regions (defined by KH93) using discrete Fourier transforms of overlapping 4-yr windows (Welch 1967) of the time series tapered with a Hanning window. Figure 3 shows the variance-preserving spectra [$fS(f)$ vs $\log(f)$] of low cloud amount, inversion strength, and SST spatially averaged over the four stratocumulus regions defined by the boxes in Fig. 2 [northeastern Pacific (NEP), northeastern Atlantic (NEA), southeastern Pacific (SEP), and southeastern Atlantic (SEA) (KH93)]. Across all four regions, there are peaks at the seasonal and diurnal cycles. Most of the variance of SST is associated with the seasonal cycle.

The seasonal cycles of all variables are weaker (especially low cloud amount) in the Northern Hemisphere stratus regions than in the Southern Hemisphere.

The spectra in Fig. 3 show that the dominant time scale of variability for low cloud amount and inversion strength is multiday rather than multimonth in the stratocumulus regions. Most of the variance of low cloud amount and inversion strength is contained in a wide band with periods between 2 and 50 days (frequency from 2×10^{-2} to $5 \times 10^{-1}\,\text{day}^{-1}$), indicating the influence of synoptic variability. Low cloud amount varies on even shorter time scales than inversion strength. The synoptic variability is mostly resolved by the multiday standard deviation, shown in Fig. 2c.

Empirical red noise spectra (dashed) are fit to the spectra in frequency bands of $1–4 \times 10^{-2}$ and $2–3 \times 10^{-1}\,\text{day}^{-1}$, away from the expected annual and daily peaks. The one-sided red noise power spectrum

$$S(f) = 2\sigma_\xi^2/[(2\pi f)^2 + \tau^{-2}] \qquad (1)$$

is appropriate for a continuous process x described by

$$\frac{\partial x}{\partial t} = \xi(t) - \tau^{-1}x, \qquad (2)$$

whose time tendency is forced by white noise $\xi(t)$ with variance σ_ξ^2, and damped with time scale τ (Munk 1960). The red noise curves fit the spectra well, excluding the diurnal and annual peaks. The damping time scale τ (days) is printed beside the curves in Fig. 3.

We expect, however, that the variance in the 2–50-day band reflects forcing that is not white, but enhanced in the synoptic band. Inversion strength variance is a factor of 2 larger than red noise at a period $f^{-1} = 10$ days in the southeastern Pacific and Atlantic, and somewhat less in the northeast regions. Synoptic variability appears stronger in the northeastern Atlantic and Pacific stratus regions. There, the red noise curve has more variance at higher frequency, and synoptic SST variance is enhanced 50% above the red noise at $f^{-1} = 10$ days. The low cloud spectral variance is dominated by synoptic variability in all the regions and by a broad peak about the diurnal cycle.

The SST is observed to vary so quickly that its empirical red noise damping time scale is much shorter than the time scale that would result from adjustment of the ocean mixed layer [e.g., 2 months for a 30-m mixed layer (Frankignoul and Hasselmann 1977)]. The strong multiday modulation of the radiative flux by low clouds ($-1\,\text{W m}^{-2}$ at 1% cloud amount) enhances the high-frequency variability of SST. The low cloud surface radiative effect due to a 25% cloud amount anomaly explains a $-0.1\,\text{K}$ response of SST to clouds persisting 10 days over a 50-m ocean mixed layer. This is about one-third of the multiday standard deviation of SST.

5. Relation of low cloud amount to inversion strength, SST, and vertical velocity

a. Inversion strength

Inversion strength explains 28% of the multiyear and 39% of the multimonth low cloud variance but only 4% of the larger multiday variance, averaged over the four KH93 eastern subtropical and tropical stratocumulus boxes. Figures 4a–e show the slope m_{cs} of the regression of low cloud amount to inversion strength for the different time scales. In Fig. 4 and subsequent figures that depend on regressions, gray crosses mark where the correlations are not significantly different from zero at 95% confidence by a Fisher's z statistic. Table 1 summarizes the slope m_{cs} averaged for each of the four stratocumulus regions. Figure 4f shows the standard deviation of inversion strength for all time scales of variability, and Figs. 4g–j show the standard deviation for each separate time scale. Inversion strength varies most on multiday time scales, with its standard deviation increasing poleward and greater than 2 K outside the tropics. Multimonth standard deviations of inversion strength reach 2 K (Fig. 4f) near the coast in the stratocumulus regions. In the deep-convective tropics (Indo-Pacific warm pool, ITCZ, and SPCZ) the inversion strength is small (Fig. 1a), and its variability is weak (<0.5 K; Figs. 4f–j).

In the southeastern Pacific stratocumulus region, the slope m_{cs} of cloud amount to inversion strength at multimonth time scales ($\sim 0.05\,\text{K}^{-1}$; Table 1) agrees with previous seasonal–regional regressions using ISCCP cloud data (Zhang et al. 2009; Sun et al. 2011) and is very close to the seasonal–regional $m_{\text{cs}} = 0.06\,\text{K}^{-1}$ from surface observations (KH93). The multimonth slope is less in the northeastern Pacific and Atlantic stratocumulus regions than the southern stratocumulus regions. The multiyear slope is approximately 0.03–0.04 K^{-1} in the southeastern subtropical oceans, slightly less than the multimonth slope.

The value of m_{cs} on multiday time scales is greater than $0.01\,\text{K}^{-1}$ in the eastern subtropical and tropical marine stratocumulus decks (Fig. 4c). The multiday slope m_{cs} of low clouds to inversion strength is negative ($-0.05\,\text{K}^{-1}$) in the tropical warm pool and intertropical convergence zone regions of significant moisture convergence, indicating low (shallow cumulus) clouds are correlated with less stable trade inversion layers. At subdaily time scales, the region of negative slope extends throughout most of the tropics, suggesting shallow
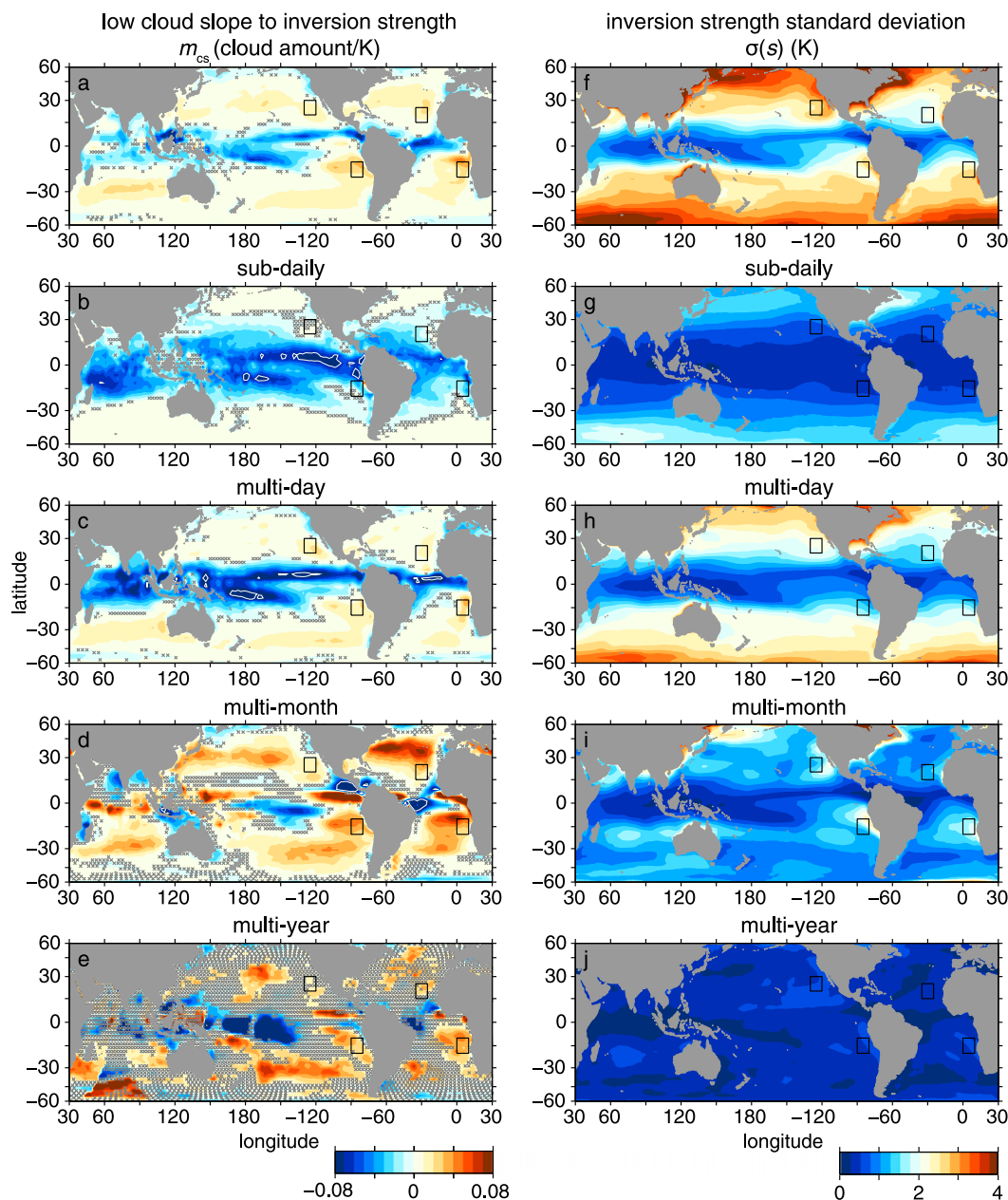
FIG. 4. (a)–(e) Response of low clouds to ERA-I inversion strength for the time scales as in Fig. A1. (f)–(j) Standard deviation of inversion strength on these time scales. Negative correlation (greater low cloud amount over cool SST anomalies) is shaded red. Locations where the correlation is not significantly different than zero by Fisher's z statistic at 95% confidence are marked with gray crosses in (a)–(e).

clouds are correlated to weak or unstable inversions on time scales of several hours (Fig. 4b).

The cloud amount response explained by inversion strength $\sigma(\hat{c}) = m_{cs}\sigma(s)$ is shown in Fig. 5, where $\sigma(s)$ is the standard deviation of the inversion strength. Over the eastern subtropical marine stratocumulus regions (around 30°N and 30°S; Figs. 5c,d), the increase of low clouds for one standard deviation of inversion strength is

stronger on multimonth time scales than on multiday time scales. The negative slope over the rest of the tropics is strongest on multiday time scales.

Figures 5f–j explore the effect of relaxing the high cloud amount and positive inversion strength sampling thresholds for the covariances. [The spatial distribution of high cloud ($p < 560$ hPa) fraction is shown in Fig. 1a.] The pattern of the response of the low clouds to

TABLE 1. Slopes m_{cs} of low cloud amount to inversion strength (% K^{-1}) averaged over the stratocumulus regions of the eastern tropical oceans, for the full variance, and for each time scale. The regional pattern of m_{cs} is shown in Fig. 4.

	NEP	SEP	NEA	SEA
Full	2.4	3.5	2.6	3.5
Subdaily	0.1	−1.6	−1.0	−1.9
Multiday	2.6	2.6	2.1	3.0
Multimonth	2.5	4.6	3.5	4.5
Multiyear	1.7	2.9	2.8	4.0

inversion strength is similar in either case. The midlatitude dipole of low cloud amount c about 45° latitude explained by inversion strength s on multiday time scales is about twice as strong when scenes with $s < 0$ and high cloud greater than 0.5 are included in the regression. This difference in midlatitudes, especially on multiday time scales, is sensitive to the sampling of high clouds. Composites of clouds and inversion strength in midlatitude cyclones explain the sign of the low cloud response to inversion strength (see the figure in the supplemental material at the Journals Online website: http://dx.doi.org/10.1175/JCLI-D-15-0460.s1). Low clouds are anticorrelated to high clouds, probably an artifact of satellite sampling. Anomalies of inversion strength are oriented nearly meridionally. The observed low cloud anomalies are slanted east-poleward and west-equatorward so that low clouds are coincident with high inversion strength equatorward of 45° latitude and with low inversion strength poleward of 45°. This differential slant of cloud and inversion strength anomalies in midlatitude cyclones explains the dipole of the cloud response in Figs. 5a,c,f,h.

Except for the eastern tropical and subtropical stratocumulus regions, the multiday standard deviation of inversion strength $\sigma(s^{day})$ is greater than the multimonth standard deviation $\sigma(s^{month})$ over most of the oceans (Figs. 4h,i) and is about twice as strong as the multimonth standard deviation in the extratropics. The multiday low cloud variations explained by inversion strength are as large as the multimonth variations explained by inversion strength (Figs. 5c,d) outside of the southeastern tropical stratocumulus decks and narrow regions on the southern flanks of the seasonally migrating northeastern Pacific and Atlantic intertropical convergence zones (ITCZs).

b. SST

SST is an important factor in determining inversion strength because the temperature of the marine boundary layer adjusts quickly to it. Radiative cooling and subsidence determine the temperature structure of the free troposphere, which in turn influences the inversion strength. We compute the slope m_{cT} of low cloud amount

to SST for multiday through multiyear time scales (Figs. 6a–d) using the daily OISSTv2 dataset. Except in the tropical convergence zones, the slope of cloud amount to SST is almost everywhere negative, indicating low clouds increase for cooler SST throughout the midlatitudes and subtropical stratus decks. On monthly and longer time scales, low cloud slope to SST closely mirrors the slope of low clouds to inversion strength, but with the opposite sign (cf. Figs. 6c,d and 4d,e). SST explains 52% of the multimonth and 30% of the multiyear inversion strength variance but only 1% of the multiday inversion strength variance. SST influences inversion strength variability on monthly and longer time scales by dominating ABL temperature variability, yet the free tropospheric temperature is set by the general circulation of the atmosphere and unlikely to be in equilibrium with local SST. The multimonth time scale (Fig. 6g) dominates the SST standard deviation (Fig. 6e). The multiday (Fig. 6f) and multiyear (Fig. 6h) standard deviation color scales are amplified by a factor of 2.

On multiday time scales, there are more low clouds for cooler SST everywhere (Fig. 6b). This partly reflects the effect of the low clouds shading the ocean surface beneath them. Figure 7, the multiday slope of SST to low cloud amount ($m_{Tc} = m_{cT} \sigma_T^2/\sigma_c^2$), shows that the ocean is cooler by −0.5°C at 100% low cloud amount (0.005°C at 1% low cloud amount) under the ITCZ and Indo-Pacific warm pool, and cooler by −1°C (at 100% low cloud amount) around 40° latitude in the northern Pacific and Atlantic subtropical mode water regions (Hanawa and Talley 2001). On day-to-day time scales, the maximum low cloud radiative effect on the surface (nominally −100 W m^{-2} at 100% cloud amount) persisting for 10 days explains a −0.4 K response for a 50-m ocean mixed layer. On monthly time scales, the boundary layer thermodynamics are in equilibrium with SST, explaining the similarity between Figs. 6c and 5d. Variability of clouds on shorter time scales, however, is out of equilibrium with the SST. On the multiday time scale, SST variations are small compared to the atmosphere and have relatively little influence on the inversion strength or cloudiness.

To examine the individual effects of SST and inversion strength on low clouds, we compare the cloud amount explained by inversion strength after removing the projection of SST (Fig. 8) with the ordinary relationship of low clouds to inversion strength (Figs. 5a,c–e). The remaining low cloud amount variability explained by inversion strength is relatively unaffected on multiday and multiyear time scales (cf. Figs. 5a,c,e with Figs. 8a,b,d). SST enhances the multimonth low cloud amount variation associated with inversion strength by a factor of 2 in the subtropical southern oceans and midlatitude northern oceans and by a factor of 3 in the
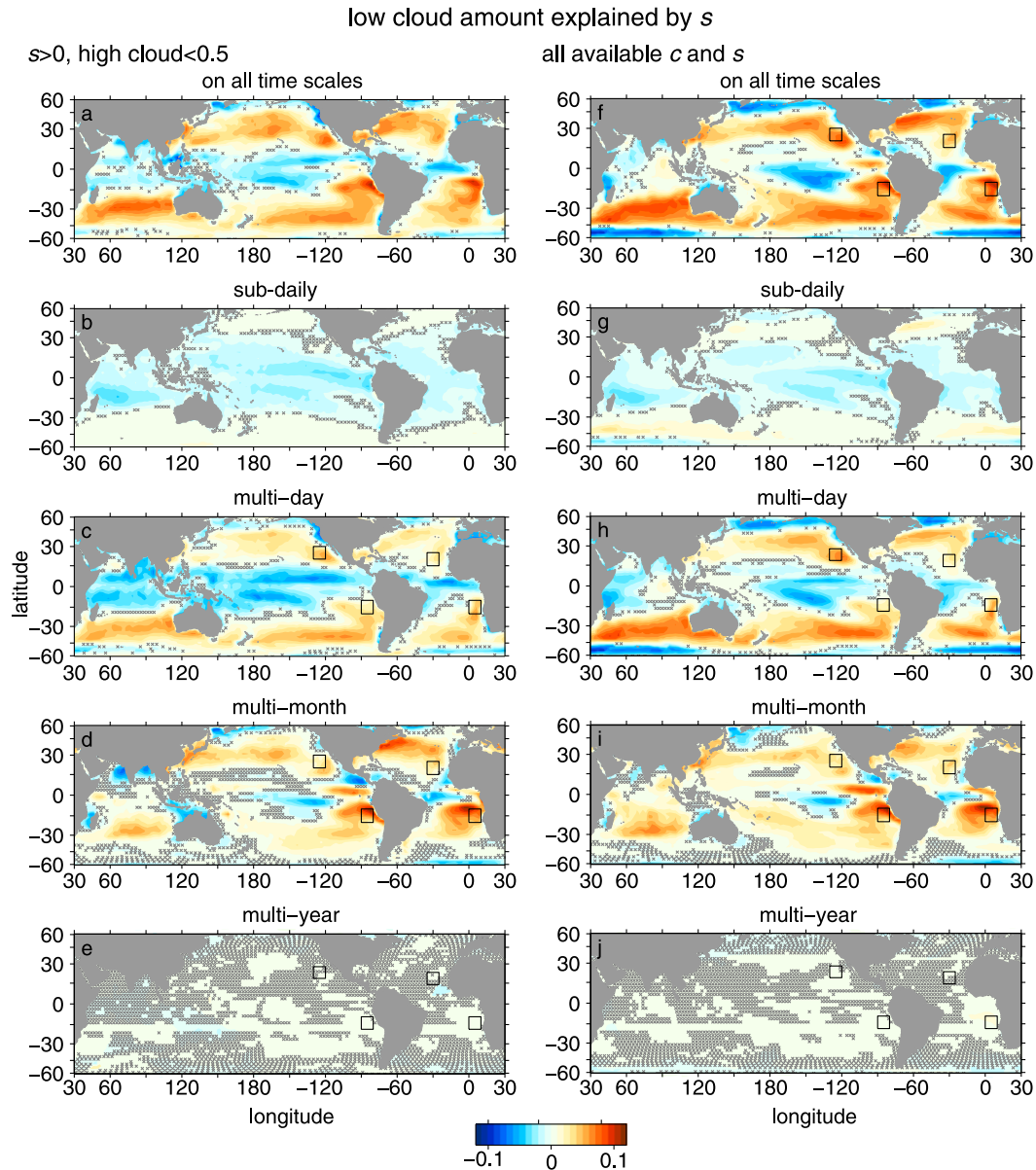
FIG. 5. Low cloud amount standard deviation explained by inversion strength s. (a)–(e) Only ISCCP scenes with positive ERA-I inversion strength ($s > 0$) and high clouds ($p < 560$ hPa) less than 0.5 are used to construct the regression. (f)–(j) All available ISCCP scenes are used to construct the regression.

southeastern tropical stratocumulus regions. The multimonth local maxima of cloud amount explained by inversion strength in the eastern tropical stratocumulus regions and the North Pacific and Atlantic Oceans (Fig. 5d) disappear once the projection of SST is removed, and inversion strength explains less than 0.04 of low cloud amount there (Fig. 8c).

c. Vertical velocity

Vertical velocity at 700 hPa ω_{700} explains 6% of the multiyear and 12% of the multimonth low cloud variance,

but only 1% of its multiday variance, averaged over the four KH93 eastern subtropical and tropical stratocumulus boxes. Figure 9 shows low cloud anomalies explained by one standard deviation of ω_{700} at each time scale, as in Figs. 5a–e, conditioned by $s > 0$, with high cloud amount less than 0.5. Negative values indicate greater low cloud amount for upward vertical motion ($\omega_{700} < 0$ Pa s^{-1}). The effect of inversion strength is retained in the regression.

Over most of the tropics, one vertical velocity standard deviation [$\sigma(\omega_{700}) \approx 0.01$ Pa s^{-1}] upward increases
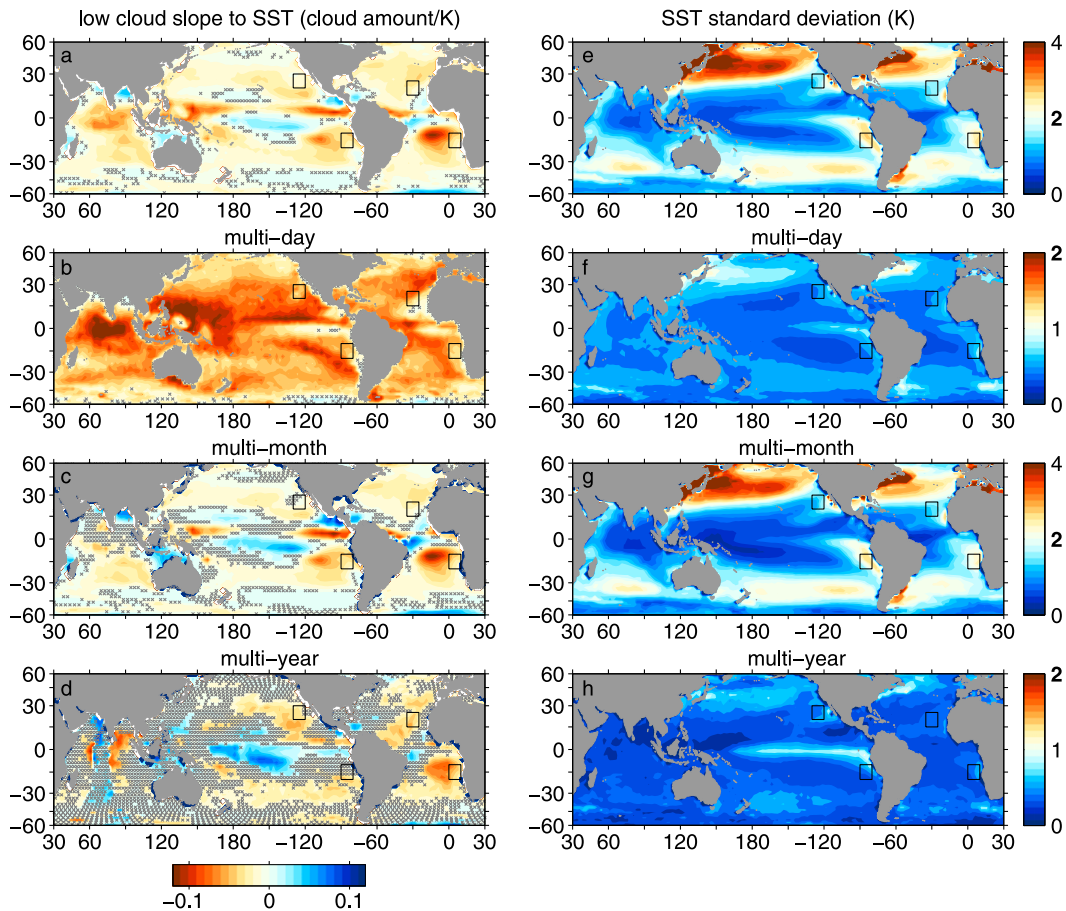
FIG. 6. As in Fig. 4, but for (a)–(d) low cloud slope to SST. The temporal sampling of the SST dataset is daily, and multiday variability is the shortest time scale considered. Negative slopes are shaded red, for comparison to Fig. 4. (right) SST (e) full, (f) multiday, (g) multimonth, and (h) multiyear standard deviation. The color scale is enhanced by a factor of two for (f) multiday and (h) multiyear standard deviation. The multiyear pattern in the Indian Ocean is unreliable because of satellite calibration artifacts.

low cloud amount by about 0.1 (Fig. 9a). In regions poleward of 40° latitude over the Southern Ocean and northwestern Pacific and Atlantic Oceans, there are more low clouds for increasing subsidence. The multiday regression dominates the total low cloud amount explained by vertical velocity for both positive and negative responses (Fig. 9c). The total low cloud amount explained by vertical velocity in the eastern tropical stratocumulus regions is weak because the subdaily low cloud response associated with subsidence (Fig. 9b) compensates the multiday low cloud response associated with ascent (Fig. 9c). Multimonth subsidence explains low cloud amount of 0.02 in the eastern tropical oceans (Fig. 9d).

Consistent with KWLJ12, positive multimonth correlations are strongest in the transition regions around 30° latitude. Negative low cloud anomalies for subsidence in the tropics (Fig. 9) disagree with KWLJ12's

nearly ubiquitous positive correlations (their Fig. 7). One hypothesis for this difference is that anomalous ascent decreases the fraction of "pure low clouds" of KWLJ12 (low clouds strictly in scenes with no middle or high clouds) more sensitively than our low cloud fraction if middle and high clouds are positively correlated to anomalous ascent, as we expect. The second hypothesis is
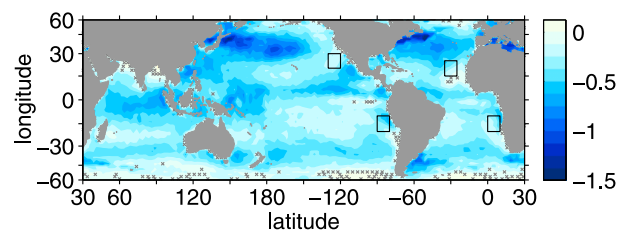

FIG. 7. The slope m_{Tc} of SST to low cloud amount variations on multiday time scales [K (100% cloud fraction)$^{-1}$].
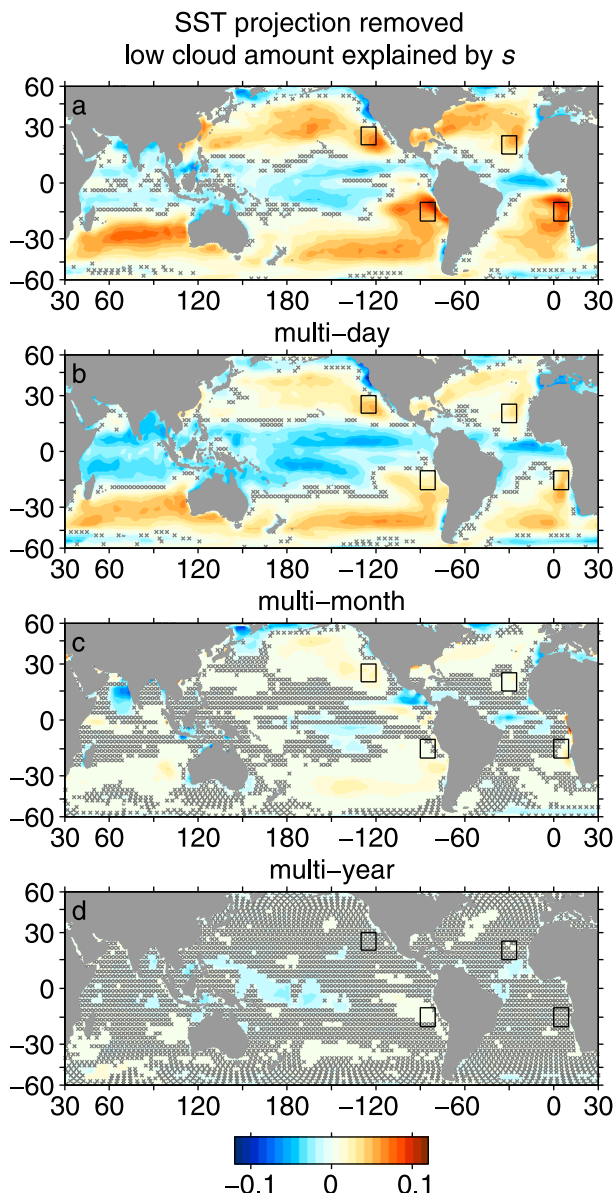
FIG. 8. As in Figs. 5b–e, but for the response of low cloud amount to inversion strength after removing the influence of SST on low cloud amount by linear regression.

FIG. 9. As in Figs. 5a–e, but the response of low clouds to one standard deviation of 700-hPa vertical pressure velocity ω_{700}. Subsiding pressure velocity is positive, so positive (red) shades represent low clouds increasing for subsidence.

that, in cumulus regimes, low (shallow cumulus) clouds themselves are associated with the same anomalous ascent as the middle and high (cumulus congestus and deep cumulus) clouds. Our more liberal counting (which differs from KWLJ12) of mixtures of low and high clouds samples this association. Low clouds in the stratocumulus regions, where high clouds are rare, have a small response to subsidence in both studies. Our pattern of low cloud explained by ω_{700} is qualitatively unchanged by requiring conditions of subsidence, or $s > 0$ and high cloud less than 0.5 (not shown).
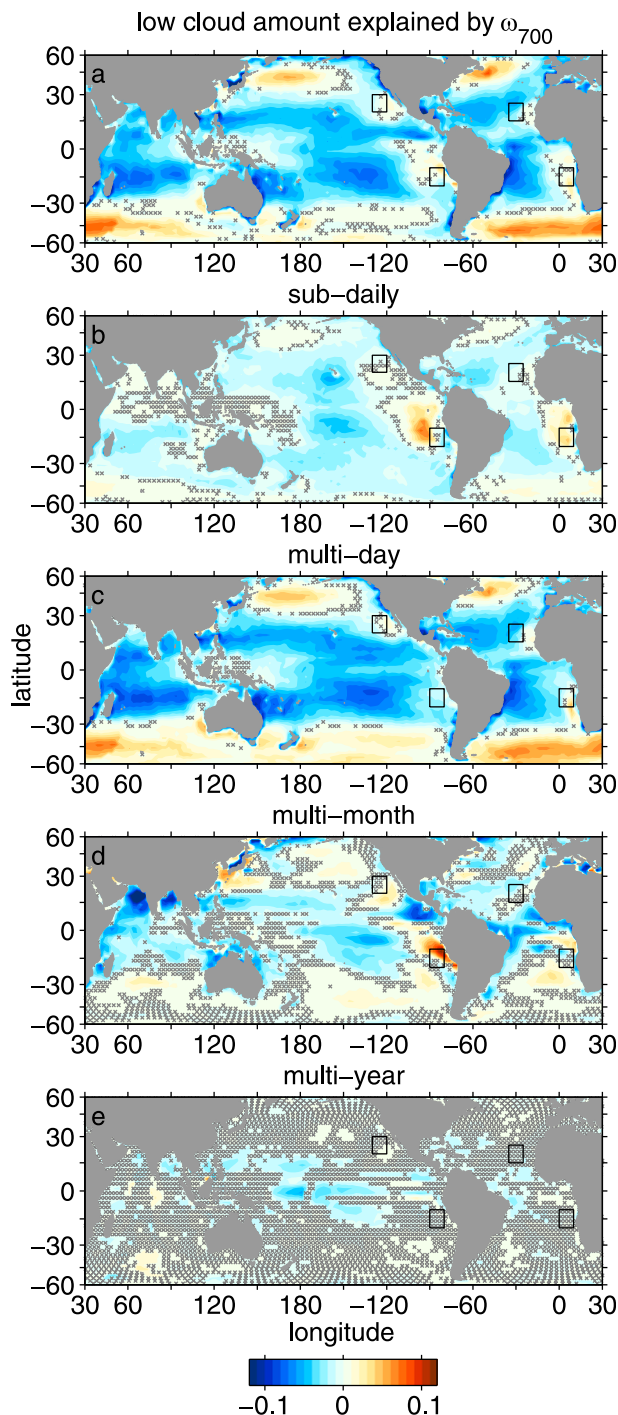
Multiyear low cloud is anticorrelated to subsidence in the central Pacific (Fig. 9e) and elsewhere does not have a significant multiyear response. The subdaily influence of subsidence in the southeastern tropical Pacific
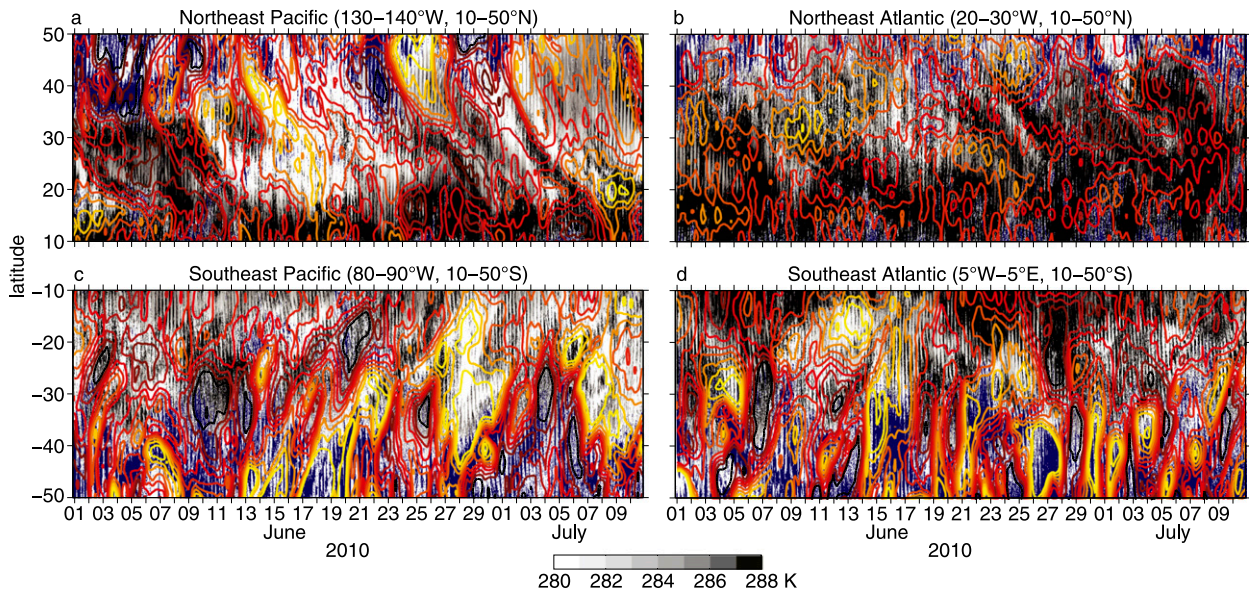
FIG. 10. Time–latitude plots of 7 km × 7 km GridSat infrared brightness temperature (IRT) indicating clouds (shaded) and ERA-I inversion strength (contoured) for 1 Jun–9 Jul 2010 (boreal summer): (a) NEP, (b) NEA, (c) SEP, and (d) SEA. IRT images of a 40° latitude × 10° longitude box are displayed every 6 h along the time axis (x axis). IRT below 273 K is shaded blue to mask high clouds. Inversion strength is contoured with an interval of 3 K in (a),(c),(d) (black contour is 0 K, maroon is 3 K, red is 6 K, orange is 9 K, and yellow is 12 K). In (b) the contour interval is 1.5 K (black contour is 1.5 K, red is 3 K, orange is 4.5 K, and yellow is 6 K).

stratocumulus region (Fig. 9b) is consistent with the effect of diurnal subsidence from a gravity wave generated by continental heating of the elevated topography of the Andes (Garreaud and Muñoz 2004; Rahn and Garreaud 2010; de Szoeke et al. 2012; Painemal et al. 2013).

Multimonth low cloud amount anomalies are associated with vertical velocity anomalies of either sign, depending on the region. Upward vertical velocity enhances convergence, deeper boundary layers, and low clouds (Myers and Norris 2013), whereas subsidence indirectly enhances clouds by enhancing inversion strength on monthly time scales. The net response of clouds to inversion strength is the balance of these. If these mechanisms are weak or nearly compensate each other, then the observed correlations between inversion strength, low clouds, and subsidence may be dominated by other factors not considered by this study. Low cloud amount explained by inversion strength looks nearly identical to Fig. 5 after subtracting the cloud anomalies explained by the 700-hPa vertical velocity (not shown).

6. Regional response of clouds to inversion strength

a. Propagation of inversion strength anomalies from the midlatitudes to the tropics

Strong day-to-day cloud variability influences even the relatively persistent eastern marine stratocumulus

decks (Fig. 2c). Synoptic variability of inversion strength is generated by midlatitude cyclones, perhaps by differential advection of the free troposphere and ABL, especially over SST gradients. Animations of clouds and inversion strength show inversion strength anomalies associated with synoptic storms deforming into narrow filaments as they wrap equatorward around the subtropical highs (see the movie in the supplemental material at the Journals Online website: http://dx.doi.org/ 10.1175/JCLI-D-15-0460.s1). These filaments travel into the regions of climatological stratocumulus cloud decks in the eastern ocean basins and modulate the size and shape of the stratocumulus cloud decks.

Figure 10 shows the meridional evolution of clouds and inversion strength over time for June–July 2010 from 10° to 50° latitude in both hemispheres. Multiple (160) 6-hourly images of 7 km × 7 km Gridded Satellite (GridSat) 11-μm infrared (IR) brightness temperature compiled from geostationary satellites (Knapp et al. 2011) are overlaid with contours of inversion strength from ERA-I. Low clouds and inversion strength anomalies copropagate equatorward in both the northern (Fig. 10a) and southern (Fig. 10c) eastern Pacific. Anomalies of clouds and inversion strength propagate equatorward faster than the mean meridional surface wind (Fig. 1d) poleward of 20° latitude. Future work is needed to clarify the roles of wave propagation and advection by anomalous winds.

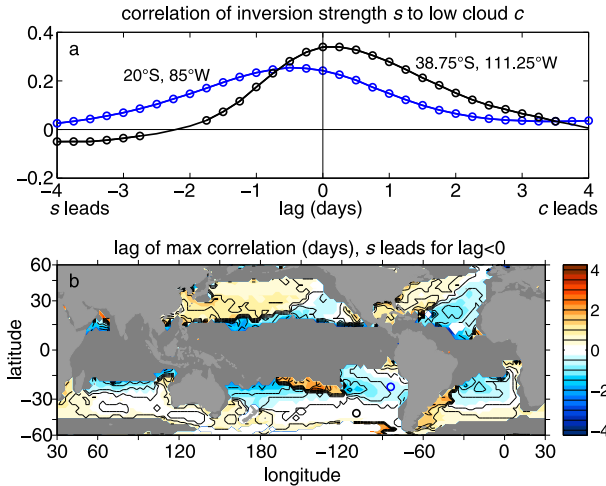FIG. 11. (a) Lag correlation between inversion strength and low cloud amount for lags between −4 and 4 days for 20°S, 85°W (blue) and 38.75°S, 111.25°W (black). Inversion strength leads low cloud for negative lags. (b) Lag of maximum correlation at every ISCCP grid location where the correlation is significant and the maximum correlation is positive. Dark gray shading over the ocean indicates regions where the strongest lag correlation between inversion strength and low cloud amount is insignificant or negative.

Low cloud anomalies associated with inversion strength propagate equatorward less clearly in the Atlantic than in the Pacific (Figs. 10b,d). Long bands of cloud and inversion strength tilt and deform in the subtropics, perhaps explaining the inconsistent meridional propagation in Fig. 10d. Clouds are few, and inversion strength is weak during summer in the northeastern Atlantic (Fig. 10b). Because the 1–2-day history of entrainment matters to the clouds, their response to synoptic variations in inversion strength may follow within the next day or two in the region downstream of the inversion strength anomalies (Xu et al. 2005; Klein et al. 1995; Mauger and Norris 2010).

b. Lag correlations

Sequences of plan-view images (see the movie in the supplemental material at the Journals Online website: http://dx.doi.org/10.1175/JCLI-D-15-0460.s1) suggest low clouds respond quickly to inversion strength anomalies on daily time scales. The temporal relationship between inversion strength anomalies and low cloud cover is illustrated by the Eulerian temporal lag correlation of low clouds and inversion strength at each ISCCP grid (Fig. 11). The lag correlations show that low cloud amount responds nearly contemporaneously with inversion strength in many places over the ocean, consistent with the Lagrangian analysis of Mauger and Norris (2010). The 1-day lag of low clouds following high lower-tropospheric stability at 30°N, 140°W corroborates results from Ocean Weather Station November (Klein

1997). Positive low cloud amount leads inversion strength by approximately 1 day in the Northern Hemisphere western midlatitude oceans (20°–50°N). Low clouds are more contemporaneously correlated with inversion strength in the Southern Hemisphere midlatitudes (30°–45°S). These relationships are due to the temporal progression of the pattern of clouds in midlatitude-propagating ridges and troughs (see the figure in the supplemental material at the Journals Online website: http://dx.doi.org/10.1175/JCLI-D-15-0460.s1). The cloud response lags inversion strength progressively more as the inversion strength anomalies propagate eastward and equatorward around the subtropical highs and into the stratocumulus regions. Inversion strength leads cloud amount by 0.5–1 day in the tropical and subtropical stratocumulus regions (e.g., at 20°S, 85°W; Fig. 11a), indicating that cloud properties respond to antecedent inversion strength anomalies (Fig. 11b).

7. Cloud-radiative feedbacks

The regressions in section 3 can be used to compute the strength of cloud-radiative feedbacks. Perturbed clouds modify the net radiation absorbed by the ocean mixed layer and ABL, further influencing the SST and ABL temperature. The feedbacks are positive if clouds are associated with cooler SST and stronger inversions. Feedbacks are based on a general mixed layer heat budget with heat capacity $\rho c_p h$ and absorbed flux F,

$$\rho c_p h (\partial T / \partial t) = F, \qquad (3)$$

where T is temperature, ρ is density, h is mixed layer thickness, and c_p is the specific heat of the substance of the mixed layer. Linearizing the dependence of the flux on mixed layer temperature $F' \cong (\partial F / \partial t) T'$ and rearranging, we define the feedback time scale:

$$\tau \equiv T' (\partial T / \partial t)^{-1} = \rho c_p h (\partial F / \partial T)^{-1}. \qquad (4)$$

First we compute the cloud radiation–SST feedback. The slope of the regression of the low cloud amount to SST is m_{cT} (Fig. 6). Clouds affect the diurnal mean net surface downwelling radiation R, which depends on the cloud amount c and the maximum (overcast) cloud-radiative effect $R_1 - R_0$, where R_0 is the clear-sky net radiation and R_1 is the net radiation for overcast clouds:

$$R = (1 - c) R_0 + c R_1 = R_0 + c (R_1 - R_0). \qquad (5)$$

We estimate the radiative effect for marine low clouds observed in the VAMOS Ocean Cloud Atmosphere Land Study Experiment (Wood et al. 2011; de Szoeke et al. 2010, 2012) as $R_{1sfc} - R_{0sfc} = -80 \, \mathrm{W \, m^{-2}}$.

The total cloud amount is $c = m_{cT}T + \tilde{c}$, where $\tilde{c}$ does not depend on T. The change in temperature of the ocean mixed layer of depth h_o depends on its heat capacity $\rho_o c_{po} h_o$. If R_{sfc} is the net surface radiation absorbed by the ocean, then the radiative heating is,

$$\rho_o c_{po} h_o \left(\frac{\partial T}{\partial t}\right)_{rad} = R_{sfc} = m_{cT}(R_{1sfc} - R_{0sfc})T + [R_{0sfc} + \tilde{c}(R_{1sfc} - R_{0sfc})]. \quad (6)$$

Subscripts o and a in the specific heat refer to the ocean surface mixed layer and atmospheric boundary layer, respectively. Since the residual cloud amount $\tilde{c}$ does not depend on SST, the term in square brackets does not affect the SST feedback. The time scale of the positive cloud radiation–SST feedback is

$$\tau_{SST} = \rho_o c_{po} h_o [m_{cT}(R_{1sfc} - R_{0sfc})]^{-1}. \quad (7)$$

Assuming the ocean mixed layer depth $h_o = 50$ m (e.g., de Boyer-Montegut et al. 2004) and low cloud amount slope to SST $m_{cT} = -0.1°C^{-1}$, the positive cloud-radiative feedback has an e-folding time scale of $\tau_{SST} = 300$ days. Even for this relatively strong estimate of the slope m_{cT}, the feedback has a much longer time scale than the less than 10-day damping time scale for SST implied by the red noise spectrum (Fig. 3).

We compare the time scale of this feedback to the time scale (4) of the restoration of the ocean mixed layer temperature by surface evaporation. The sensible heat flux is constant, assuming constant sea–air temperature difference ΔT. Assuming constant relative humidity RH, the evaporation depends on the change in saturation vapor pressure q_s with SST. Linearizing about SST, the derivative of the surface evaporation with respect to SST is $\partial E/\partial T = \rho_a C_H UL[(1 - RH)(\partial q_s/\partial T) + RH(\partial^2 q_s/\partial T^2)\Delta T]$. The SST feedback time scale is estimated from (4) as,

$$\tau_{SST,evap} = \rho_o c_{po} h_o (\partial E/\partial T)^{-1} = \rho_o c_{po} h_o \left\{\rho_a C_H UL\left[(1 - RH)\frac{\partial q_s}{\partial T} + RH\frac{\partial^2 q_s}{\partial T^2}\Delta T\right]\right\}^{-1}. \quad (8)$$

For SST = 20°C, bulk heat transfer coefficient $C_H = 1.1 \times 10^{-3}$, wind speed $U = 5$ m s^{-1}, latent heat of vaporization $L = 2.5 \times 10^6$ J kg^{-1}, $\Delta T = 1.5°C$, and RH = 80%, the negative surface evaporation feedback is 500 days, slightly weaker than the positive radiative SST feedback.

Though the cloud radiation–SST feedback has been found to amplify the mean seasonal and interannual meridional asymmetry of the northern-ITCZ southern stratus deck couplet in general circulation models of the eastern Atlantic and Pacific Oceans (e.g., Philander et al. 1996; Ma et al. 1996; Xie 2005; de Szoeke et al. 2006; Bellomo et al. 2014, 2015), faster processes on time scales less than 300 days drive most of the observed SST variability.

We estimate the atmospheric cloud radiation–ABL temperature feedback from the radiative heating of the ABL. This mechanism is physically distinct from the cloud radiation–SST feedback, but since SST and inversion strength are correlated, our empirical estimates of the slopes m_{cs} and m_{cT} of clouds to inversion strength and SST are not independent.

Clouds modulate the net radiative divergence between the surface and the inversion as in (5). The net radiative loss of energy due to clouds cools the ABL, increasing its relative humidity and cloud amount. The effect of ABL temperature on saturation and the effect of stability-reducing entrainment are both included in the slope of low cloud to inversion strength m_{cs}. Liquid water potential temperature θ_{lABL} is conserved in the ABL. Assuming

free-tropospheric temperature anomalies are uncorrelated, anomalies of θ'_{lABL} are closely related to inversion strength anomalies $s' = -\theta'_{lABL}$ The ABL radiative heating is

$$\rho_a c_{pa} h_{ABL} \left(\frac{\partial \theta'_{lABL}}{\partial t}\right)_{rad} = -m_{cs}\theta'_{lABL}(R_{1ABL} - R_{0ABL})_0^{h_{ABL}} + [R_{0ABL} + \tilde{c}(R_{1ABL} - R_{0ABL})], \quad (9)$$

where ρ_a, c_{pa}, and h_{ABL} represent properties of air affecting the boundary layer heat capacity. The residual cloud amount $\tilde{c}$ does not depend on θ_{lABL}, so the term in square brackets does not affect the feedback. The cloud radiation–ABL temperature feedback time scale is

$$\tau_{rad,ABL} = -\rho_a c_{pa} h_{ABL}/m_{cs}(R_{1ABL} - R_{0ABL}). \quad (10)$$

On balance, clouds radiate more net longwave radiation from the boundary layer top than they warm the atmospheric boundary layer due to solar absorption, resulting in a net cooling of $R_{1ABL} - R_{0ABL} = -50$ W m^{-2} when clouds are present.[1] We estimate the cloud-radiative feedback e-folding time scale $\tau_{rad,ABL} = 14$ days for a typical

---

[1] The Exner function relating potential temperature to temperature amplifies the effect of cloud-top radiative heating on θ_{lABL} by +5%. The inversion strength is reduced about −4% by latent heating in the cloud. We neglect these two opposing minor effects.

slope $m_{cs} = 0.02\,\mathrm{K}^{-1}$ (Fig. 4) and ABL depth $h_{ABL} = 1200\,\mathrm{m}$. The time scale of the cloud radiation–ABL temperature feedback is therefore considerably faster (the feedback is stronger) than the positive cloud radiation–SST feedback, but not fast enough to overcome the 1–2-day damping time scale due to the surface and entrainment fluxes of temperature and moisture into the ABL. For entrainment $w_e = 4\,\mathrm{mm\,s}^{-1}$ and $5\,\mathrm{m\,s}^{-1}$ for surface wind speed, the equilibration time scale for the ABL adjustment to the fluxes is 1.5 days (Schubert et al. 1979). The 14-day time scale of the cloud radiation–ABL temperature feedback suggests that it might be responsible for amplifying the variability of low clouds on synoptic (especially multiweek) and longer time scales (Fig. 2).

8. Summary

KH93 analyzed the climatological seasonal cycle of low cloud amount among different regions, finding a slope of +0.06 low cloud amount per kelvin lower-tropospheric stability (LTS) among regions and seasons. Previous regressions with ISCCP data give low cloud–LTS slopes of +0.05 (Zhang et al. 2009), consistent with the slope in our monthly regressions. On time scales shorter than a day and in tropical regions of atmospheric convergence and warm SST, low clouds increase for weaker inversions.

Even in the stratocumulus regions, where the seasonal influence of lower-tropospheric stability on low clouds is well established, day-to-day time scales dominate low cloud amount variance. Low cloud variability averaged over the four subtropical and tropical stratocumulus regions has significant peaks at the seasonal and diurnal cycle (11% of variance is at $f < 0.01\,\mathrm{day}^{-1}$ and 28% at $f > 0.5\,\mathrm{day}^{-1}$), yet 61% of variance is in a broad band from 2 to 100 days (Fig. 3). Multiday low cloud variance over the midlatitudes and subtropics is largely correlated to inversion strength (Fig. 5). Most inversion strength variance (50%) is on multiday time scales (40% is multimonth, 5% is subdaily, and 4% is multiyear). Multiyear inversion strength anomalies do not explain significant low cloud variations.

The response of clouds to vertical motion also depends on the time scale and region. Subdaily low cloud amount increases with subsidence only in the southeastern Pacific and Atlantic stratocumulus regions. Especially over the southeastern Pacific Ocean, this correlation may be due to fortuitous coincidence of diurnal cloud clearing by solar warming of the cloud top and the downward phase of a diurnal gravity wave generated by continental heating (e.g., Garreaud and Muñoz 2004). On multimonth time scales, low clouds in the eastern tropical stratocumulus decks are also correlated with subsidence (without controlling for inversion strength). Away from the stratocumulus cloud decks, clouds increase for ascent in the free troposphere,

presumably because shallow cumulus clouds, also counted as low clouds in our analysis, are enhanced by low-level convergence. On multiday time scales, these shallow clouds increase approximately 5% on average for one (upward) standard deviation of 700-hPa pressure velocity.

Low clouds are anticorrelated with subsidence on multiday time scales, but positively correlated on multimonth time scales. On multiday time scales, the nonlocal meteorological history experienced by the boundary layer is important (Klein et al. 1995), and trajectories show subsidence is anticorrelated to low cloud amount on daily time scales (Mauger and Norris 2010). Subsidence can strengthen the inversion by slowly warming the air capping the inversion. Subsidence also limits the height of the boundary layer and the ability for boundary layer air to reach saturation. KWLJ12 find the correlation of low clouds to vertical velocity (and SST) increases when daily data are averaged with 15-day running means. The apparent multimonth correlation of low clouds is probably due to the association of subsidence with inversion strength. Controlling for the effect of inversion strength, clouds increase for upward motion even on monthly time scales (Myers and Norris 2013).

Midlatitude synoptic intrusions affect subtropical low clouds in the northeastern hemisphere winter associated with anomalous cold advection and poleward sea level pressure ridges (Klein 1997; Rozendaal and Rossow 2003). Northwestward propagation of microphysical and macrophysical cloud properties is associated with large-scale patterns of pressure variability in the southeastern Pacific (George and Wood 2010). Multiday inversion strength anomalies propagate from midlatitudes to the tropics, especially over the eastern Pacific Ocean. A 1-month anecdote from austral winter shows equatorward copropagation of low cloud and inversion strength anomalies from midlatitudes toward the southeastern and northeastern Pacific stratocumulus regions (Fig. 10). Anomalies propagate less clearly over the Atlantic. We suspect these anomalies propagate into the stratocumulus regions by a combination of wave processes and advection.

Cold SST is ubiquitously correlated with low clouds on multiday time scales (Fig. 6b). This is probably because of the shading effect of clouds on the ocean heat budget. SST decreases 0.1°–1°C, depending on region, for a 100% change in low cloud fraction. This relationship of SST to low cloud amount at multiday time scales is consistent with the cooling expected of an ocean mixed layer experiencing cloud-radiative cooling.

SST varies most on multimonth time scales, mostly because of the repeating seasonal cycle. SST variability contributes to low clouds in the southeastern Pacific and Atlantic stratocumulus regions, but its influence is weak in the northeastern stratocumulus regions. Low clouds

increase by $0.05\,\mathrm{K}^{-1}$ SST for multimonth and multiyear time scales over the deep tropics near the date line and decrease over the cooler eastern oceans, subtropics, and midlatitudes. SST is responsible for enhancing the multimonth low cloud amount explained by inversion strength to 0.05 over much of the northern midlatitude and southern subtropical oceans and to 0.1 in the southern tropical stratocumulus regions. Removing the effect of SST, the multimonth low cloud amount explained by inversion strength is everywhere 0.03 or less.

The sensitivities of low clouds to SST and to inversion strength imply positive cloud-radiative feedbacks that amplify variability of the boundary layer temperature and SST. A more stable inversion reduces entrainment by raising the energetic cost of entraining warmer air. With weaker entrainment, the boundary layer becomes moister, and the cloud amount increases. The clouds shade the ocean surface from sunlight and cool the SST. The ABL responds to SST relatively quickly, increasing the inversion strength and relative humidity for a cool SST anomaly. The adjustment time scale of the SST to the solar flux anomaly is about 300 days. This positive feedback may be responsible for low-frequency variability of SST and low clouds in the eastern Pacific and Atlantic (Clement et al. 2011; Evan et al. 2013; Bellomo et al. 2014, 2015).

The cloud radiation–ABL feedback results from the effect of emissive clouds on the net radiative divergence from the atmospheric boundary layer. It amplifies longer-than-weekly synoptic variability with an *e*-folding time scale of 14 days. The ABL radiative feedback is 20 times stronger as a result of the small heat capacity of the ABL $(1.3 \times 10^6\,\mathrm{J\,K}^{-1}\,\mathrm{m}^{-2})$ compared to the ocean mixed layer $(2.1 \times 10^8\,\mathrm{J\,K}^{-1}\,\mathrm{m}^{-2})$. Both positive cloud-radiative feedbacks are weaker than the surface and entrainment flux damping of the ABL, so cloud-radiative feedbacks do not completely destabilize the ABL cloud system.

The response of climate models to greenhouse gas forcing depends strongly on their representation of low clouds, yet these models simulate low clouds and their sensitivities poorly. Common cloud and ocean surface heat flux errors in the eastern ocean stratocumulus regions develop on time scales of hours to days in climate models, for reasons that differ between models (Medeiros et al. 2012; Toniazzo and Woolnough 2014). Reproducing observed low cloud variability, including its strong multiday variability and its statistical relations to SST and inversion strength, is a test of the cloud physics of climate models.

Several results advance our understanding of clouds: Inversion strength does not reliably predict low cloud amount on time scales shorter than a day, precluding it from being used in parameterizations of low clouds on the time step of a general circulation model. Low cloud amount is anticorrelated to inversion strength over tropical low-level

convergent regions on daily time scales and anticorrelated equatorward of 30° latitude on time scales shorter than a day. In the eastern Pacific and Atlantic stratocumulus regions, low cloud variance explained by multiday inversion strength is about half that explained by multimonth inversion strength. Finally, day-to-day variations dominate low cloud variance, even where the seasonal low cloud relationship to stability holds, so the effect of weather on low clouds is likely to affect Earth's climate.

APPENDIX A

Separation of Calendar Time Scales by Window Averages

Cloud amount, vertical velocity, and inversion strength are sampled at 6-h intervals. SST is sampled daily. These time series are decomposed into yearly, monthly, daily, and 6-hourly anomalies. The averaging windows are defined by the civil calendar (UTC):

$$x = \overline{x} + x^{\mathrm{year}} + x^{\mathrm{month}} + x^{\mathrm{day}} + x^{\mathrm{6h}}. \qquad \text{(A1)}$$

The $\overline{x}$ represents the record mean of x. The window anomaly x^{Δ_i} for window length Δ_i and next longer window length Δ_{i+1} is defined:

$$x^{\Delta_i} = [x]^{\Delta_i} - [x]^{\Delta_{i+1}}. \qquad \text{(A2)}$$

The brackets represent time averages over windows of length Δ_i. Our window anomalies are then

$$
\begin{aligned}
x^{\mathrm{year}} &= [x]^{\mathrm{year}} &&- \overline{x}, \\
x^{\mathrm{month}} &= [x]^{\mathrm{month}} &&- [x]^{\mathrm{year}}, \\
x^{\mathrm{day}} &= [x]^{\mathrm{day}} &&- [x]^{\mathrm{month}}, \quad \text{and} \\
x^{\mathrm{6h}} &= x &&- [x]^{\mathrm{day}}.
\end{aligned}
\qquad \text{(A3)}
$$

The window-average anomalies are mutually orthogonal for the different window lengths. Thus, upon squaring (A1), the variance of x is the sum of the variances of the anomalies at the separate time scales:

$$\overline{x'x'} = \overline{x^{\mathrm{year}}x^{\mathrm{year}}} + \overline{x^{\mathrm{month}}x^{\mathrm{month}}} + \overline{x^{\mathrm{day}}x^{\mathrm{day}}} + \overline{x^{\mathrm{6h}}x^{\mathrm{6h}}}. \qquad \text{(A4)}$$
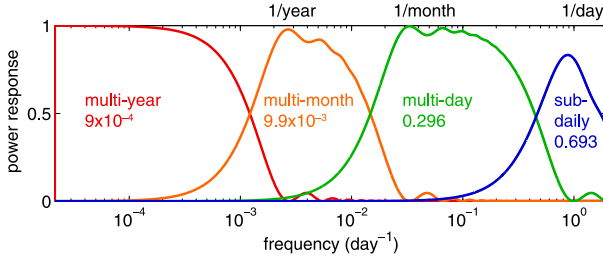
FIG. A1. Spectral response of yearly (red), monthly (orange), daily (green), and 6-hourly (blue) averaging windows. Numbers shown indicate the fraction of power resolved by each window-averaged component of a white time series.

The window averages bandpass filter the time series. The spectral power response for each window average $[\sin(\pi\Delta f)/(\pi\Delta f)]$ for the rectangular window of length Δ (Blackman and Tukey 1958)] is shown in Fig. A1. A power response of 1 means all signal power at that frequency passes through the window average. Except at the poorly resolved high frequencies, the sum of the power response for all window-average anomalies at a given frequency yields 1. If the original time series had equal variance at all frequencies, then the subdaily window average would resolve 69% of its variance, the multiday band 30%, and the multimonth band 1%. The multiyear band would resolve a tiny fraction (9×10^{-4}) of its variance.

APPENDIX B

Regression

Our terminology for standard regressions follows. We define, for instance, the low cloud amount anomaly c' with respect to its mean $\bar{c}$:

$$c = \bar{c} + c', \tag{B1}$$

so $\overline{c'} = 0$. The cloud anomaly c' is written as the sum of a part $\hat{c} = m_{cs}s'$ correlated to inversion strength s (with slope m_{cs} of the regression line of c vs s) and a part a' uncorrelated to s:

$$c' = m_{cs}s' + a'. \tag{B2}$$

Multipling (B2) by s' and averaging yields the slope

$$m_{cs} = \overline{c's'}/\overline{s's'}. \tag{B3}$$

The standard deviation of c is $\sigma(c) = \overline{c'c'}^{1/2}$. Squaring and averaging (B2) shows the variance $\sigma^2(c) = \overline{c'c'}$ of cloud amount is the sum of the variance of the cloud amount explained by s and the variance uncorrelated to s:

$$\overline{c'c'} = m_{cs}^2\overline{s's'} + \overline{a'a'}. \tag{B4}$$

Digital datasets containing variances and covariances of total cloud, low cloud, inversion strength, 700-hPa pressure velocity, and SST suitable for calculating slopes and fractions of variance explained by each variable are available as supplemental material at the Journals Online website: http://dx.doi.org/10.1175/JCLI-D-15-0460.s2.

REFERENCES

Bellomo, K., A. C. Clement, T. Mauritsen, G. Rädel, and B. Stevens, 2014: Simulating the role of subtropical stratocumulus clouds in driving Pacific climate variability. *J. Climate*, **27**, 5119–5131, doi:10.1175/JCLI-D-13-00548.1.

——, ——, ——, ——, and ——, 2015: The influence of cloud feedbacks on equatorial Atlantic variability. *J. Climate*, **28**, 2725–2744, doi:10.1175/JCLI-D-14-00495.1.

Blackman, R. B., and J. W. Tukey, 1958: The measurement of power spectra from the point of view of communications engineering—Part I. *Bell Syst. Tech. J.*, **37**, 185–282, doi:10.1002/j.1538-7305.1958.tb03874.x.

Bony, S., and J.-L. Dufresne, 2005: Marine boundary layer clouds at the heart of tropical cloud feedback uncertainties in climate models. *Geophys. Res. Lett.*, **32**, L20806, doi:10.1029/2005GL023851.

Clement, A. C., R. Burgman, and J. R. Norris, 2009: Observational and model evidence for positive low-level cloud feedback. *Science*, **325**, 460–464, doi:10.1126/science.1171255.

——, P. DiNezio, and C. Deser, 2011: Rethinking the ocean's role in the Southern Oscillation. *J. Climate*, **24**, 4056–4072, doi:10.1175/2011JCLI3973.1.

de Boyer Montégut, C., G. Madec, A. S. Fischer, A. Lazar, and D. Iudicone, 2004: Mixed layer depth over the global ocean: An examination of profile data and a profile-based climatology. *J. Geophys. Res.*, **109**, C12003, doi:10.1029/2004JC002378.

Dee, D. P., and Coauthors, 2011: The ERA-Interim reanalysis: Configuration and performance of the data assimilation system. *Quart. J. Roy. Meteor. Soc.*, **137**, 553–597, doi:10.1002/qj.828.

de Szoeke, S. P., Y. Wang, S.-P. Xie, and T. Miyama, 2006: Effect of shallow cumulus convection on the eastern Pacific climate in a coupled model. *Geophys. Res. Lett.*, **33**, L17713, doi:10.1029/2006GL026715.

——, C. W. Fairall, D. E. Wolfe, L. Bariteau, and P. Zuidema, 2010: Surface flux observations on the southeastern tropical Pacific Ocean and attribution of SST errors in coupled ocean–atmosphere models. *J. Climate*, **23**, 4152–4174, doi:10.1175/2010jcli3411.1.

——, S. Yuter, D. Mechem, C. W. Fairall, C. D. Burleyson, and P. Zuidema, 2012: Observations of stratocumulus clouds and their effect on the eastern Pacific surface heat budget along 20°S. *J. Climate*, **25**, 8542–8567, doi:10.1175/JCLI-D-11-00618.1.

Evan, A. T., R. J. Allen, R. Bennartz, and D. J. Vimont, 2013: The modification of sea surface temperature anomaly linear damping time scales by stratocumulus clouds. *J. Climate*, **26**, 3619–3630, doi:10.1175/JCLI-D-12-00370.1.

Frankignoul, C., and K. Hasselmann, 1977: Stochastic climate models. Part II: Application to sea-surface temperature anomalies and thermocline variability. *Tellus*, **29A**, 289–305, doi:10.1111/j.2153-3490.1977.tb00740.x.

Garreaud, R. D., and R. Muñoz, 2004: The diurnal cycle in circulation and cloudiness over the subtropical southeast Pacific: A modeling study. *J. Climate*, **17**, 1699–1710, doi:10.1175/1520-0442(2004)017<1699:TDCICA>2.0.CO;2.

George, R. C., and R. Wood, 2010: Subseasonal variability of low cloud radiative properties over the southeast Pacific Ocean. *Atmos. Chem. Phys.*, **10**, 4047–4063, doi:10.5194/acp-10-4047-2010.

Hanawa, K., and L. D. Talley, 2001: Mode waters. *Ocean Circulation and Climate—Observing and Modelling the Global Ocean*, G. Siedler, J. Church, and J. Gould, Eds., International Geophysics Series, Vol. 77, Academic Press, 373–386, doi:10.1016/S0074-6142(01)80129-7.

ISCCP Science Team, 1999: ISCCP D1. NASA Atmospheric Science Data Center, accessed July 2013, doi:10.5067/ISCCP/D1.

Klein, S. A., 1997: Synoptic variability of low-cloud properties and meteorological parameters in the subtropical trade wind boundary layer. *J. Climate*, **10**, 2018–2039, doi:10.1175/1520-0442(1997)010<2018:SVOLCP>2.0.CO;2.

——, and D. L. Hartmann, 1993: The seasonal cycle of low stratiform clouds. *J. Climate*, **6**, 1587–1606, doi:10.1175/1520-0442(1993)006<1587:TSCOLS>2.0.CO;2.

——, ——, and J. R. Norris, 1995: On the relationships among low-cloud structure, sea surface temperature, and atmospheric circulation in the summertime northeast Pacific. *J. Climate*, **8**, 1140–1155, doi:10.1175/1520-0442(1995)008<1140:OTRALC>2.0.CO;2.

Knapp, K. R., and Coauthors, 2011: Globally gridded satellite observations for climate studies. *Bull. Amer. Meteor. Soc.*, **92**, 893–907, doi:10.1175/2011BAMS3039.1.

Kubar, T. L., D. E. Waliser, J.-L. Li, and X. Jiang, 2012: On the annual cycle, variability, and correlations of oceanic low-topped clouds with large-scale circulation using *Aqua* MODIS and ERA-Interim. *J. Climate*, **25**, 6152–6174, doi:10.1175/JCLI-D-11-00478.1.

Lauer, A., K. Hamilton, Y. Wang, V. T. J. Phillips, and R. Bennartz, 2010: The impact of global warming on marine boundary layer clouds over the eastern Pacific—A regional model study. *J. Climate*, **23**, 5844–5863, doi:10.1175/2010JCLI3666.1.

Loeb, N. G., B. A. Wielicki, D. R. Doelling, G. L. Smith, D. F. Keyes, S. Kato, N. Manalo-Smith, and T. Wong, 2009: Toward optimal closure of the Earth's top-of-atmosphere radiation budget. *J. Climate*, **22**, 748–766, doi:10.1175/2008JCLI2637.1.

Ma, C.-C., C. R. Mechoso, A. W. Robertson, and A. Arakawa, 1996: Peruvian stratus clouds and the tropical Pacific circulation: A coupled ocean–atmosphere GCM study. *J. Climate*, **9**, 1635–1645, doi:10.1175/1520-0442(1996)009<1635:PSCATT>2.0.CO;2.

Mauger, G. S., and J. R. Norris, 2010: Assessing the impact of meteorological history on subtropical cloud fraction. *J. Climate*, **23**, 2926–2940, doi:10.1175/2010JCLI3272.1.

Medeiros, B., D. L. Williamson, C. Hannay, and J. G. Olson, 2012: Southeast Pacific stratocumulus in the Community Atmosphere Model. *J. Climate*, **25**, 6175–6192, doi:10.1175/JCLI-D-11-00503.1.

Munk, W. H., 1960: Smoothing and persistence. *J. Meteor.*, **17**, 92–93, doi:10.1175/1520-0469(1960)017<0092:SAP>2.0.CO;2.

Myers, T. A., and J. R. Norris, 2013: Observational evidence that enhanced subsidence reduces subtropical marine boundary layer cloudiness. *J. Climate*, **26**, 7507–7524, doi:10.1175/JCLI-D-12-00736.1.

Norris, J. R., 2000: What can cloud observations tell us about climate variability? *Space Sci. Rev.*, **94**, 375–380, doi:10.1023/A:1026704314326.

——, 2005: Multidecadal changes in near-global cloud cover and estimated cloud cover radiative forcing. *J. Geophys. Res.*, **110**, D08206, doi:10.1029/2004JD005600.

——, and A. T. Evan, 2015: Empirical removal of artifacts from the ISCCP and PATMOS-x satellite cloud records. *J. Atmos. Oceanic Technol.*, **32**, 691–702, , doi:10.1175/JTECH-D-14-00058.1.

Painemal, D., P. Minnis, and L. O'Neill, 2013: The diurnal cycle of cloud-top height and cloud cover over the southeastern Pacific as observed by *GOES-10*. *J. Atmos. Sci.*, **70**, 2393–2408, doi:10.1175/JAS-D-12-0325.1.

Philander, S. G. H., D. Gu, D. Halpern, G. Lambert, N. C. Lau, T. Li, and R. C. Pacanowski, 1996: Why the ITCZ is mostly north of the equator. *J. Climate*, **9**, 2958–2972, doi:10.1175/1520-0442(1996)009<2958:WTIIMN>2.0.CO;2.

Rahn, D. A., and R. Garreaud, 2010: Marine boundary layer over the subtropical southeast Pacific during VOCALS-REx—Part 1: Mean structure and diurnal cycle. *Atmos. Chem. Phys.*, **10**, 4491–4506, doi:10.5194/acp-10-4491-2010.

Rasch, P. J., and J. E. Kristjánsson, 1998: A comparison of the CCM3 model climate using diagnosed and predicted condensate parameterizations. *J. Climate*, **11**, 1587–1614, doi:10.1175/1520-0442(1998)011<1587:ACOTCM>2.0.CO;2.

Reynolds, R. W., T. M. Smith, C. Liu, D. B. Chelton, K. S. Casey, and M. G. Schlax, 2007: Daily high-resolution-blended analyses for sea surface temperature. *J. Climate*, **20**, 5473–5496, doi:10.1175/2007JCLI1824.1.

Risen, C. M., and D. B. Chleton, 2008: A global climatology of surface wind and wind stress fields from eight years of QuikSCAT scatterometer data. *J. Phys. Oceanogr.*, **38**, 2379–2413, doi:10.1175/2008JPO3881.1.

Rossow, W. B., and R. A. Schiffer, 1999: Advances in understanding clouds from ISCCP. *Bull. Amer. Meteor. Soc.*, **80**, 2261–2287, doi:10.1175/1520-0477(1999)080<2261:AIUCFI>2.0.CO;2.

Rozendaal, M. A., and W. B. Rossow, 2003: Characterizing some of the influences of the general circulation on subtropical marine boundary layer clouds. *J. Atmos. Sci.*, **60**, 711–728, doi:10.1175/1520-0469(2003)060<0711:CSOTIO>2.0.CO;2.

——, C. B. Leovy, and S. A. Klein, 1995: An observational study of diurnal variations of marine stratiform cloud. *J. Climate*, **8**, 1795–1809, doi:10.1175/1520-0442(1995)008<1795:AOSODV>2.0.CO;2.

Schubert, W. H., J. S. Wakefield, E. J. Steiner, and S. K. Cox, 1979: Marine stratocumulus convection. Part I: Governing equations and horizontally homogeneous solutions. *J. Atmos. Sci.*, **36**, 1286–1307, doi:10.1175/1520-0469(1979)036<1286:MSCPIG>2.0.CO;2.

Sun, F., A. Hall, and Q. Xu, 2011: On the relationship between low cloud variability and lower tropospheric stability in the Southeast Pacific. *Atmos. Chem. Phys.*, **11**, 9053–9065, doi:10.5194/acp-11-9053-2011.

Toniazzo, T., and S. Woolnough, 2014: Development of warm SST errors in the southern tropical Atlantic in CMIP5 decadal hindcasts. *Climate Dyn.*, **43**, 2889–2913, doi:10.1007/s00382-013-1691-2.

——, S. J. Abel, R. Wood, C. R. Mechoso, G. Allen, and L. C. Shaffrey, 2011: Large-scale and synoptic meteorology in the south-east Pacific during the observations campaign VOCALS-REx in austral Spring 2008. *Atmos. Chem. Phys.*, **11**, 4977–5009, doi:10.5194/acp-11-4977-2011.

Tselioudis, G., W. B. Rossow, and D. Rind, 1992: Global patterns of cloud optical thickness variation with temperature. *J. Climate*, **5**, 1484–1495, doi:10.1175/1520-0442(1992)005<1484:GPOCOT>2.0.CO;2.

Welch, P. D., 1967: The use of fast Fourier transform for the estimation of power spectra: A method based on time averaging

over short, modified periodograms. *IEEE Trans. Audio Electroacoust.*, **15**, 70–73, doi:10.1109/TAU.1967.1161901.

Wielicki, B. A., B. R. Barkstrom, E. F. Harrison, R. B. Lee, G. Louis Smith, and J. E. Cooper, 1996: Clouds and the Earth's Radiant Energy System (CERES): An Earth Observing System experiment. *Bull. Amer. Meteor. Soc.*, **77**, 853–868, doi:10.1175/1520-0477(1996)077<0853:CATERE>2.0.CO;2.

Wood, R., and C. S. Bretherton, 2006: On the relationship between stratiform low cloud cover and lower-tropospheric stability. *J. Climate*, **19**, 6425–6432, doi:10.1175/JCLI3988.1.

——, and Coauthors, 2011: The VAMOS ocean-cloud-atmosphere-land study regional experiment (VOCALS-REx):

Goals, platforms, and field operations. *Atmos. Chem. Phys.*, **11**, 627–654, doi:10.5194/acp-11-627-2011.

Xie, S.-P., 2005: The shape of continents, air–sea interaction, and the rising branch of the Hadley circulation. *The Hadley Circulation: Past, Present and Future*, H. F. Diaz and R. S. Bradley, Eds., Kluwer Academic Publishers, 121–152.

Xu, H., S.-P. Xie, and Y. Q. Wang, 2005: Subseasonal variability of the southeast Pacific stratus cloud deck. *J. Climate*, **18**, 131–142, doi:10.1175/JCLI3250.1.

Zhang, Y., B. Stevens, B. Medeiros, and M. Ghil, 2009: Low-cloud fraction, lower-tropospheric stability, and large-scale divergence. *J. Climate*, **22**, 4827–4844, doi:10.1175/2009JCLI2891.1.